A&A 429, 713–730 (2005)
DOI: 10.1051/0004-6361:20041667

Astronomy & Astrophysics

Polarization of the Sun's continuous spectrum

J. O. Stenflo[1,2]

[1] Institute of Astronomy, ETH Zentrum, 8092 Zurich, Switzerland
e-mail: stenflo@astro.phys.ethz.ch
[2] Faculty of Mathematics & Science, University of Zurich, 8057 Zurich, Switzerland

Received 15 July 2004 / Accepted 9 September 2004

Abstract. The Sun's spectrum is linearly polarized by coherent scattering processes. Here we develop the theory for the formation of the polarized continuum, identify the relevant physical mechanisms, and clarify their relative roles. The polarized photons are produced by scattering at neutral hydrogen in its ground state (Lyman scattering), and to a smaller degree by scattering at free electrons (Thomson scattering). The polarized photons are diluted by the unpolarized photons from the H^- opacity and radiative absorption from the Balmer bound-bound and bound-free transitions. Due to pressure broadening of the Balmer lines from the statistical Stark effect the polarized Balmer jump is shifted from the series limit to substantially longer wavelengths. In the second part of the paper the Atlas of the Second Solar Spectrum that covers 3161−6995 Å for disk position $\mu = 0.1$ (where μ is the cosine of the heliocentric angle) is used to extract the empirical values of the continuum polarization with the help of a model for the behavior of the depolarizing lines. The empirically determined continuum polarization lies systematically lower than the values that have been predicted for $\lambda > 4000$ Å from radiative-transfer modelling. The Balmer jump is found to be shifted as expected from pressure-broadening theory. Through scaling of the relative center-to-limb variations obtained from radiative-transfer theory with the empirically determined values (valid for $\mu = 0.1$) we finally obtain the semi-empirical function that describes the variation of the continuum polarization with both wavelength and disk position μ. The empirically determined continuum polarization can be used to constrain model atmospheres as well as to fix the zero point of the polarization scale in observations of the scattering polarization and the Hanle effect.

Key words. polarization – scattering – Sun: photosphere – atomic processes – techniques: polarimetric – radiation mechanisms: general

1. Introduction

The Sun's spectrum is linearly polarized by coherent scattering processes. This polarization is largest near the solar limb due to the more favorable scattering geometry there, but systematic exploration of the scattering polarization has only become possible during the last decade with the availability of sufficiently sensitive polarimetric instrumentation (Povel 1995). The polarized spectrum turns out to be as richly structured as the unpolarized intensity spectrum, but since the appearance of the polarized structures and their physical origins are very different from the structures in the intensity spectrum, we are actually dealing with a new and complementary spectrum of the Sun. The polarization spectrum formed by coherent scattering has therefore been called the "Second Solar Spectrum" (Ivanov 1991; Stenflo & Keller 1997).

The Second Solar Spectrum is characterized by a polarized continuous background, on which a rich variety of both intrinsically polarizing and depolarizing lines are superposed. While the depolarizing lines have the appearance of "absorption" lines, the polarizing lines look like "emission" lines. Many lines however belong to an intermediate category if they are only weakly polarizing, or if their line polarization is partially depolarized by magnetic fields via the Hanle effect. The appearance of the Second Solar Spectrum actually varies with the phase of the solar cycle, since the Hanle effect depolarization is more pronounced at activity maximum due to the larger amounts of hidden magnetic flux in the Sun's atmosphere (cf. Berdyugina et al. 2002). To properly interpret the line polarization and the Hanle effect one needs to know the level of the continuum polarization background and understand how this background is formed (cf. Stenflo et al. 1998).

Unfortunately the level of the continuous polarization cannot presently be determined as precisely as the relative polarization variations in the spectrum (for which a polarimetric precision of 10^{-5} is routinely achieved). Slight asymmetries in the bidirectional charge shifts within the demodulating ZIMPOL detector and instrumental polarization cause zero-point offsets of the polarization scale. These effects can be calibrated, but currently not to the same polarimetric precision as that of the relative polarization scale. For practical purposes the zero point offset therefore has to be treated as an unknown free parameter, while the relative variations are well determined. If the level of the continuous polarization were known from other investigations, then this knowledge could be applied to fix the zero point of the polarization scale for any polarimetric recording (that includes a portion of the continuum). The present paper aims at finding the functional dependence of the continuum

polarization with respect to both wavelength and disk position (represented by μ, the cosine of the heliocentric angle).

Various attempts were made in the 1970s to measure the continuum polarization and its center-to-limb variation (Leroy 1972; Mickey & Orral 1974; Wiehr 1975). They have been reviewed by Leroy (1977). Although these broad-band and non-imaging observations allowed a general verification of theoretical concepts for the origin of the continuum polarization that had been developed in the pioneering works of Débarbat et al. (1970) and Dumont & Pecker (1971), they are not of sufficient accuracy, wavelength coverage and resolution to allow a good quantitative comparison with detailed radiative-transfer modelling. Such modelling has provided us with theoretical values for the continuum polarization over the wavelength range 4000–8000 Å (Fluri & Stenflo 1999), but the theory has not been applied below 4000 Å. The UV is the most interesting wavelength region, since the continuum polarization increases steeply with decreasing wavelength, and there is interesting physics occuring around the Balmer jump.

With the availability of the new Atlas of the Second Solar Spectrum, which covers the wavelength range 3161–6995 Å in three volumes (Gandorfer 2000, 2002, 2004), we now have a comprehensive data set with which we may in principle extract the values for the continuum polarization. Since however the zero point of the polarization scale is unknown in the Atlas, the extraction procedure needs to make use of a model for the behavior of the depolarizing lines. A similar approach was applied to the first survey of the Second Solar Spectrum more than two decades ago (Stenflo et al. 1983a,b), but the polarimetric accuracy at that time did not allow the scale of the continuum polarization to be determined with much confidence, in contrast to the present situation.

The present data set covers a wide wavelength range, where many different physical mechanisms come into play. As previous theoretical work (Débarbat et al. 1970; Fluri & Stenflo 1999) has focused on the radiative-transfer aspects of the problem, we find a need to elucidate the underlying physics in a more systematic and transparent way. Therefore we develop in the first part of the paper the theory that governs the formation of the polarized continuum, identify the various contributing mechanisms, and clarify their respective roles. In the second part we extract the empirical values of the continuum polarization from the Atlas data and compare them with the theoretical predictions, to examine to what extent some physics is missing. The empirical values are finally connected with radiative-transfer modelling to obtain the semi-empirical function that gives the continuum polarization for all wavelengths and disk positions μ.

2. Theoretical formulation

2.1. Classical theory

In the classical picture the atoms are treated as radiatively damped classical oscillators with resonant frequency ω_0 and damping rate γ, governed by equation

$$\frac{\mathrm{d}^2 x_q}{\mathrm{d}t^2} + \gamma \frac{\mathrm{d}x_q}{\mathrm{d}t} + \omega_0^2 x_q = -\frac{e}{m} E'_q, \tag{1}$$

where E'_q is the electric field of the incident radiation. $q = 0, \pm 1$ is the index for the three vector components. The orthogonal basis of choice is not Cartesian coordinates but complex spherical vectors, representing one linear polarization ($q = 0$, the π component), and two circular polarizations ($q = \pm 1$, the σ components). Only with this choice of basis vectors do the three component equations stay uncoupled when a magnetic field is introduced (although in the following we will only be dealing with the zero-field case). These vector components correspond to the magnetic substates in the quantized picture.

The oscillating electric vector E'_q induces an oscillating dipole moment d_q per unit volume. The stationary oscillatory solution of Eq. (1) is

$$d_q = -Nex_q = \epsilon_0 E'_q (n_q^2 - 1), \tag{2}$$

where N is the number of oscillators per unit volume, $-e$ the electron charge, ϵ_0 the permeability of vacuum, and n_q the component of the refractive index for the medium of oscillators. In the non-magnetic case $n_q = n$, i.e., independent of q. While time-dependent theory is needed to treat line-broadening effects (cf. Bommier & Stenflo 1999), it is sufficient here to limit the discussion to the stationary solutions.

The non-magnetic refractive index n is given by

$$n^2 - 1 = \frac{\omega_A^2}{\omega_0^2 - \omega^2 - i\,\gamma\,\omega}, \tag{3}$$

where ω is the frequency of the incident radiation, and

$$\omega_A = \sqrt{\frac{e^2 N}{\epsilon_0\, m}} \tag{4}$$

would be the standard plasma frequency if N were equal to N_e, the electron density. Instead of an ordinary plasma of non-resonant free electrons, we are here dealing with a "plasma" of resonant oscillators.

The excited oscillators emit dipole radiation. From the classical expression for dipole radiation one can derive an expression for the relation between d_q and the electric vector E_q of the emitted radiation. Together with Eq. (2) one then gets a relation between the exciting electric field E'_q and the scattered electric field E_q, which, when transformed to a basis of linear polarization vectors (which is the natural basis for measuring devices), can be expressed in terms of the Jones scattering matrix. From the tensor product of two Jones scattering matrices one obtains the Mueller scattering matrix that describes how the incident Stokes vector $\boldsymbol{I}'$ is transformed to the scattered Stokes vector $\boldsymbol{I}$. The normalization condition for the Mueller scattering matrix leads to the definition and expression for the scattering cross section σ. For details of all these derivations we refer to a relevant monograph (Stenflo 1994).

The result is

$$\sigma = \frac{\omega^4}{\pi c^4}\,\frac{2}{3}\,\left|\frac{1}{2}(n^2 - 1)\right|^2. \tag{5}$$

The factor of $\frac{2}{3}$ comes from the angular averaging of the geometrical factors in the normalization condition for the Mueller

scattering matrix. The squaring of $n^2 - 1$ occurs because bilinear products of Jones matrices are used to form the Mueller matrix.

Inserting Eqs. (3) and (4) in Eq. (5) we obtain

$$\sigma = N\sigma_{\rm e}\,\frac{\omega^4}{4\omega_0^2}\,\left|\frac{1}{\omega_0-\omega-i\gamma/2}\;+\;\frac{1}{\omega_0+\omega+i\gamma/2}\right|^2, \qquad (6)$$

where $\sigma_{\rm e}$ is, as we will see below, the Thomson scattering cross section per electron, and is given by

$$\sigma_{\rm e} = \frac{8\pi}{3}\,r_{\rm e}^2, \qquad (7)$$

where

$$r_{\rm e} = \frac{e^2}{4\pi\epsilon_0 mc^2} \qquad (8)$$

is the classical electron radius. Since $r_{\rm e} = 2.818\times10^{-15}$ m, it follows that $\sigma_{\rm e} = 6.653\times10^{-29}$ m^2.

It is interesting to note that Eq. (6) contains one resonant and one non-resonant term, which have exactly the same form as in the Kramers-Heisenberg scattering theory. In quantum electrodynamics these two terms are interpreted in terms of time ordering of the Feynman diagrams. Thus the resonant term represents absorption followed by emission, while the non-resonant term represents the seemingly strange process of emission followed by absorption. Since the classical theory is not a perturbation theory, it produces automatically both terms without the need for any intriguing time-ordering interpretations.

If the oscillating medium would have resonances at several frequencies other than ω_0, which were coherently excited by the same driving electric field E'_q of the incident radiation, then we would get a linear superposition of the Jones matrices for the various resonances. Due to the bilinear multiplications between the Jones matrices when forming the Mueller matrix, we would then get interference terms between scattering amplitudes belonging to different resonant frequencies. We will see explicitly in the quantum-mechanical formulation how such interferences must occur because the intermediate state is a mixed quantum state (linear superposition of all possible intermediate states).

In the limit of vanishing damping constant we obtain

$$\sigma = N\sigma_{\rm e}\,\frac{\omega^4}{(\omega_0^2-\omega^2)^2}. \qquad (9)$$

Here we see that in the special case when the resonant frequency is zero (i.e., no resonance at all), as we have with free electrons,

$$\sigma = \sigma_{\rm T} = N\sigma_{\rm e}, \qquad (10)$$

where $\sigma_{\rm T}$ is the Thomson cross section for scattering at free electrons.

2.2. Derivation in terms of the Einstein coefficients

The phenomenological use of transition rates given by the Einstein coefficients is conceptually simple and a convenient way to find the magnitude of the scattering cross section, but this approach cannot properly deal with quantum interferences or polarization. Still, because of its simplicity and transparency, it helps to illuminate the physics.

This approach conceptually views scattering as a two-step process: radiative excitation, followed by spontaneous emission. Let us label the initial, intermediate, and final states by indices i, e, and f, respectively. To make the treatment more general, we allow i and f to be different (Raman scattering). $i = f$ then represents the special case of Rayleigh scattering. The incident frequencies are ν_i (or $\omega_i = 2\pi\nu_i$), the scattered frequencies ν_f.

The coefficient of radiative absorption is, for a given resonant transition $i \rightarrow e$,

$$\kappa_{ie} = N_i\,B_{ie}\,\frac{h\nu_i}{4\pi}\,\varphi_\nu, \qquad (11)$$

where B_{ie} is the Einstein coefficient for radiative absorption, N_i the number density of atoms in state i, and φ_ν is an area-normalized profile function.

Of all the radiatively excited atoms, only the fraction ρ_{ef} that represents spontaneous emission from level e to level f constitutes the scattering transition under consideration.

$$\rho_{ef} = A_{ef}\Big/\sum_j R_{ej}, \qquad (12)$$

where R_{ej} stands for the total transition rate (radiative plus collisional) from e to j, and we have to sum over all possible states j. ρ_{ef} is thus a branching ratio, while $\sum_j R_{ej}$ is the effective damping rate γ or inverse life time of level e (although it does not include the damping from elastic collisions, which is important for line-broadening theory).

The scattering cross section σ represents the product of the absorption cross section and the branching ratio. Thus

$$\sigma = \kappa_{ie}\,A_{ef}/\gamma. \qquad (13)$$

Introducing the absorption oscillator strength f_{ie} and the statistical weights g_i, g_e, and g_f for the various states, and making use of the Einstein relations between the transition rates, we get

$$\begin{aligned} B_{ie} &= \frac{2\pi^2e^2}{\epsilon_0\,c\,h\,m\,\omega_{ei}}\,f_{ie},\\ A_{ef} &= \frac{2h\nu_f^3}{c^2}\,B_{ef},\\ B_{ef} &= \frac{g_f}{g_e}\,B_{fe}, \end{aligned} \qquad (14)$$

where $\omega_{ei} = (E_e - E_i)/\hbar$ is the resonant frequency of the absorption transition (while ω_{ef} represents the emission transition). With Eqs. (11) and (13) this gives

$$\sigma = N_i\,\sigma_e\,\omega_i\,\omega_f^3\,\frac{3g_f}{g_e}\,\frac{f_{ie}}{\omega_{ei}}\,\frac{f_{fe}}{\omega_{ef}}\,\frac{\varphi_\nu}{4\gamma}. \tag{15}$$

From this derivation we see how the factor $\omega_i\omega_f^3$ arises: ω_i relates to the energy of the absorbed photons, while ω_f^3 comes from the expression for spontaneous emission and can be seen as representing the energy density (zero-point energy) of the vacuum.

In standard non-LTE theory, φ_ν is (in the frame of the atom) taken to be the Lorentz profile:

$$\varphi_\nu = \frac{\gamma}{(\omega_{ef} - \omega_f)^2 + (\gamma/2)^2}. \tag{16}$$

To dispel any confusion about a factor of 2π in the above expression we note that the normalization of φ_ν is with respect to $\int \mathrm{d}\nu = \int \mathrm{d}\omega/\,2\pi$, not with respect to $\int \mathrm{d}\omega$.

If we define

$$\Phi_\nu = \frac{2/i}{\omega_{ef} - \omega_f - i\gamma/2}, \tag{17}$$

then we see that

$$\varphi_\nu = \mathrm{Re}\,\Phi_\nu. \tag{18}$$

We further easily verify that φ_ν can be converted to a product:

$$\varphi_\nu = \frac{\gamma}{4}\,\Phi_\nu\,\Phi_\nu^*. \tag{19}$$

According to quantum-mechanical perturbation theory (see below), one needs to add a non-resonant term to Φ_ν in Eq. (17), so that we instead use

$$\Phi_\nu = \frac{2}{i}\left(\frac{1}{\omega_{ef} - \omega_f - i\gamma/2} + \frac{1}{\omega_{ei} + \omega_f + i\gamma/2}\right). \tag{20}$$

While this extra term, which represents emission followed by absorption in the Feynman diagram interpretation, is unimportant in the neighborhood of the resonance, it is essential for the continuum polarization, which receives its contributions from the distant line wings, far from the resonances. As has been pointed out in the preceding section, this extra, non-resonant term follows automatically from the standard classical theory and must be used at frequencies far from the resonances.

The correspondence with the classical theory is now manifest. The classical theory corresponds to an $S \rightarrow P \rightarrow S$ transition without electron spin, where $\omega_{ei} = \omega_{ef} = \omega_0$, $f_{ie} = f_{fe} = 1$, $\omega_i = \omega_f$, $g_f = 1$, and $g_e = 3$ (the three m states of the excited P state, or, classically, the three spherical vector components of the oscillation, with $q = 0, \pm 1$). Inserting these values in Eq. (15), we retrieve precisely the classical scattering cross section, as required by the correspondence principle.

2.3. Quantum-mechanical scattering

The phenomenological treatment in terms of transition rates gives us the correct Raman scattering cross section for a single scattering transition, but it does not include the quantum interferences between all the possible excited states that are involved in scattering from i to f, and it cannot deal with the polarizability of a scattering transition. For this we need the quantum-mechanical perturbation theory. For the scattering cross section this theory gives the same results as Eqs. (15)–(20), except that we need to sum over all the possible excited states before forming the product of the profile functions.

Let us for convenience define a generalized profile function as follows:

$$\psi_e = \frac{\sqrt{g_i\,g_f\,f_{ie}\,f_{fe}}}{\sqrt{\omega_{ei}\;\omega_{ef}}} \times\left(\frac{1}{\omega_{ef} - \omega_f - i\gamma/2} + \frac{1}{\omega_{ei} + \omega_f + i\gamma/2}\right). \tag{21}$$

$g = 2J + 1$ is the statistical weight for each total angular momentum state J (or F in the case of hyperfine structure splitting). Further,

$$N_i = \frac{g_i}{\sum_{J_i} g_{J_i}}\,N, \tag{22}$$

where N is the total population of all the fine-structure components with total angular momentum J_i of the initial, lower state, while the scattering transition that we consider refers to one particular J_i value (here represented by index i in N_i). We then get

$$\sigma = \frac{N}{\sum_{J_i} g_{J_i}}\,\frac{1}{4}\,\sigma_e\,\omega_i\,\omega_f^3\sum_{J_e}\frac{3}{2J_e+1}\left|\sum_{n_e}\psi_e(n_e, J_e)\right|^2. \tag{23}$$

We notice two types of summation in this expression: (1) a coherent summation of the generalized profile functions, done before the squaring is performed, and carried out over the radial quantum number $n = n_e$ of the excited state e while the total angular momentum quantum number J_e is kept fixed; (2) an incoherent summation (done after the squaring has taken place) over all the possible total angular momentum substates of the excited state. The reason why the sum over J_e is not part of the coherent summation is that for the scattering opacity, in contrast to the scattering polarizability (see below), algebraic calculations show that there is no quantum interference between states of different angular momentum (cf. Stenflo 1994, p. 194; Stenflo 1997, Eq. (12)), only between states of equal angular momentum but different radial quantum number n.

2.4. Polarizability

The polarizability of a scattering transition is characterized by the parameter W_2, which represents the fraction of the scattering transitions that behave like classical, dipole-type scattering in terms of polarization and angular dependence (as given by the Mueller phase matrix). The remaining fraction, $1 - W_2$, behaves like isotropic, unpolarized scattering.

Let us generalize the scattering cross section σ by introducing σ_K, where σ_0 is identical to our previous σ and the polarizability W_2 can be expressed as

$$W_2 = \sigma_2/\sigma_0. \tag{24}$$

The expression for σ_K can be written

$$\begin{aligned}\sigma_K \;=\; & \frac{N}{\sum_{J_i}(2J_i+1)}\,\frac{1}{4}\,\sigma_e\,\omega_i\,\omega_f^3 \\ & \times \sum_{J_{e_1},J_{e_2}} 9\,c\,(J_i,\,J_f)^{(K)}_{J_{e_1}-J_i,\,J_{e_2}-J_i} \\ & \times \sum_{L_{e_1},L_{e_2}} (-1)^{r_{ie_1}+r_{ie_2}+r_{fe_1}+r_{fe_2}} \\ & \times \sum_{n_{e_1},n_{e_2}} \psi_e(n_{e_1},\,L_{e_1},\,J_{e_1})\,\psi_e^*(n_{e_2},\,L_{e_2},J_{e_2}).\end{aligned} \tag{25}$$

With these expressions we obtain the polarizability W_2 from Eq. (24). The coefficients $c(J_i,\,J_f)^{(K)}_{J_{e_1}-J_i,\,J_{e_2}-J_i}$ have been derived and given explicitly in terms of simple algebraic functions of J_i in Stenflo (1997). The factor of 9 is needed here because of the way in which these coefficients were defined in Stenflo (1997). It allows us to use, without modifications, the expressions of that paper. r_{ie} is an integer that determines the sign of the expression. It depends on the values of $\Delta L = L_e - L_i$ and $\Delta J = J_e - J_i$ in a way specified in detail in Stenflo (1994, 1997), where these parameters were introduced. The sign can only become negative if $i \neq f$ (Raman scattering). For Rayleigh scattering the entire sign factor can therefore be omitted.

Index K represents the $2K$-multipole. $K = 0$ relates to the unpolarized intensity, $K = 2$ to the atomic alignment. The circumstance that σ_0 is identical to our previous scattering cross section σ implies that

$$9\,c\,(J_i,\,J_f)^{(0)}_{J_e-J_i,\,J_e-J_i} \;=\; \frac{3}{2J_e+1}, \tag{26}$$

as can be verified from the algebraic expressions in Stenflo (1997). In addition, as noted in the previous subsection, the $c^{(0)}$ coefficients are only non-zero when $J_{e_1} = J_{e_2}$. In this isotropic case, where there is no interference between states of different total angular momentum, the sign factor is always +1 and can accordingly be omitted. The sign factor therefore only needs to be considered in the interference terms for the alignment represented by σ_2, and then only for Raman scattering when $i \neq f$.

If several different types of opacity sources are present, then the effective polarizability of the medium is obtained by summing over the various opacity and alignment contributions labeled with summation index j:

$$W_{2,\,\mathrm{eff}} = \sum_j \sigma_{2,\,j} \Big/ \sum_j \sigma_{0,\,j}. \tag{27}$$

2.5. Limb darkening and the last scattering approximation

The amount of continuum polarization in the emergent radiation depends on the effective polarizability $W_{2,\,\mathrm{eff}}$ of Eq. (27) and on the scattering geometry, in particular on the anisotropy of the incident radiation field and the viewing angle. Since the relative magnitudes of the various opacity sources depend on temperature and density, $W_{2,\,\mathrm{eff}}$ is height dependent. As the radiation anisotropy is also height dependent and the medium optically thick (multiple scattering), the full radiative transfer problem needs to be solved numerically to obtain the continuum polarization correctly.

It is however possible to obtain good estimates of the amount of scattering polarization by using the idealization of the *last scattering approximation*. Since the polarization amplitudes that we are dealing with are very small (a fraction of one percent), the polarization of the incident radiation at the last scattering event can be disregarded. It is thus assumed that the polarization of the emergent radiation is created in a single scattering event (the last one) rather than through multiple scattering. The only thing we then need to know, besides $W_{2,\,\mathrm{eff}}$, is the anisotropy of the incident radiation field that the last scattering event sees.

Our next idealization is to let this anisotropy be given by the observed limb darkening function at the considered wavelength. This is not quite correct, since the observed limb darkening refers to zero optical depth, whereas most of the observed photons originate at line-of-sight optical depth unity, or vertical optical depth μ, where μ is the cosine of the heliocentric angle. This difference however becomes small at the extreme limb, where μ goes to zero, since there the radiation comes from the top of the atmosphere (in the plane-parallel approximation). As $W_{2,\,\mathrm{eff}}$ varies with height, we have to choose a value that is representative for the height (around optical depth μ) from where the bulk of the continuum photons come.

Thus, at least for order of magnitude estimates, we expect the continuum polarization to scale with the product $k_G W_{2,\,\mathrm{eff}}$, where k_G is a geometric depolarization factor that depends on the viewing angle and describes the dilution of the polarization due to the angular integration over the incident radiation. For pure 90° scattering we would have $k_G = 1$. In the last scattering approximation we obtain k_G by multiplying the Rayleigh phase matrix with an unpolarized Stokes vector and integrating over all incident angles. As shown in Stenflo (1982), we then obtain

$$k_G(\mu) = G\,(1-\mu^2)\,/I_\nu(\mu), \tag{28}$$

where

$$G = \frac{3}{16}\int_{-1}^{1}(1-3\mu'^2)\,I_\nu(\mu')\,\mathrm{d}\mu'. \tag{29}$$

For convenience, and with sufficient accuracy within the context of our present idealizations, we use the following analytic representation of the limb darkening function,

$$I_\nu(\mu)/I_\nu(1.0) = 1 - u - v + u\mu + v\mu^2, \tag{30}$$

since the empirically determined fit parameters u and v have been tabulated by Pierce (2000) from 2000 Å to 1 μm. The expression is valid for positive μ only. For negative μ we set $I_\nu(\mu) = 0$, since Eq. (30) represents the surface, where the radiation field is only in the outwards direction. With this limb darkening function,

$$G = \frac{3}{64}\,u + \frac{1}{20}\,v. \tag{31}$$

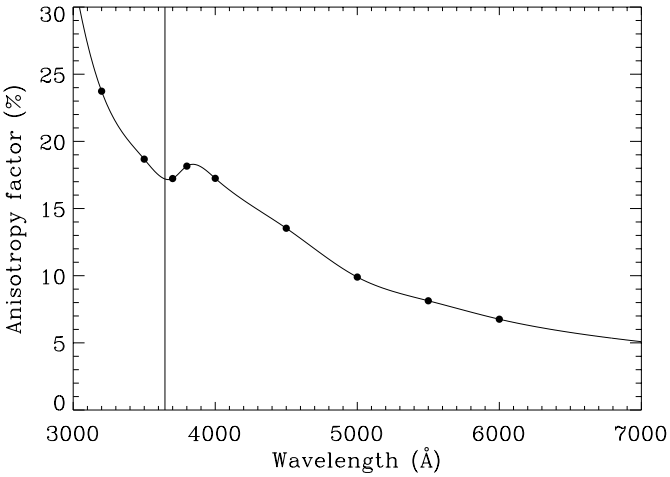

Fig. 1. Wavelength dependence of the anisotropy factor k_G for $\mu = 0.1$. Note that the effective Balmer jump occurs at substantially longer wavelengths than the actual series limit (marked by the vertical line).

k_G as calculated from the tabulation of u and v for $\mu = 0.1$ (which is the standard limb distance used in most recordings of the scattering polarization, like for the three atlas volumes of the Second Solar Spectrum by Gandorfer 2000, 2002, 2004) is given in Fig. 1. The filled circles refer to the rather widely spaced wavelengths, for which u and v have been tabulated. The smooth, solid curve has been obtained through spline interpolation between these points. It is striking how k_G increases towards shorter wavelengths, from 5% at 7000 Å, to more than 30% at 3000 Å, because the limb darkening is enhanced when going from the red to the blue. Note also the signature of the Balmer jump in the radiation anisotropy and how it is shifted to considerably longer wavelengths than the actual series limit (marked by the vertical line in the figure). The main physical cause for this shift will be described in Sect. 3.6.

While this idealized treatment provides a good description of how the anisotropy and the continuum polarization vary with wavelength, it does not give a good description of the center-to-limb variation of the polarization. One reason for this is that the scattering opacity is confined to an optically thin layer, most of which lies above the non-polarizing region where the bulk of the continuum intensity originates. Therefore the relative proportion of polarized scattered photons to all photons scales with the optical thickness in the viewing direction of the scattering layer, i.e., in proportion to $1/\mu$. The relative center-to-limb variation of the scattering polarization is therefore expected to have the approximate analytical form $(1-\mu^2)/\mu$, and will be given in greater detail in Sect. 4.4 below. At the extreme limb, where the scattering layer becomes optically thick, our idealization for k_G may be more valid, but it is clear that we should use it with caution, as a tool to elucidate the basic physical mechanisms without having to enter into the realm of radiative transfer computations.

3. Scattering at hydrogen

The by far dominating contribution to the continuum opacity at optical wavelengths on the Sun comes from hydrogen. We can distinguish between unpolarized and polarizing opacity contributions. Unpolarized contributions come from the H^- opacity and from bound-bound and bound-free radiative absorption that is not part of a scattering process. The polarizing contributions are due to scattering from initial levels $n = 1$ (Lyman scattering) and $n = 2$ (Balmer scattering). In addition, there are contributions from Thomson scattering at free electrons.

Lyman scattering at visible wavelengths occurs in the dispersion wings of the Lyman series lines, very far from the respective resonance frequencies. The opacity in the visible is attenuated by the great distance from these resonances, and is approximately proportional to $(\omega/\omega_0)^4$ (cf. Eq. (9)), where ω_0 is the center of gravity of the resonances in the Lyman series. In contrast, Balmer scattering in the visible occurs in the midst of the contributing resonances, which are distributed across the visible range. The Balmer scattering contribution is however attenuated by the population factor $N_{n=2}/N_{n=1}$. Quantitative comparison of these attenuation factors (see below) shows that the Balmer scattering contribution to the visible continuum is much smaller than the Lyman contribution.

3.1. Oscillator strengths and Gaunt factors

To evaluate the expressions for the scattering opacity and polarizability in hydrogen, we need the oscillator strengths of all the possible transitions, both the bound-bound and bound-free. For bound-bound transitions in hydrogen between lower level n' and upper level n, the absorption oscillator strength is

$$f_{n'n} = G_{\rm I}\, f'_{n'n}, \tag{32}$$

where $f'_{n'n}$ is given by a simple algebraic expression due to Kramers (1923),

$$f'_{n'n} = \frac{2^6}{3\sqrt{3}}\,\frac{1}{g_{n'}}\,\frac{1}{\left(\frac{1}{n'^2}-\frac{1}{n^2}\right)^3}\left|\frac{1}{n^3}\,\frac{1}{n'^3}\right|, \tag{33}$$

and $G_{\rm I}$ is the dimensionless Gaunt factor of order unity for the bound-bound case. Tables of the bound-bound oscillator strengths have been given by Wiese et al. (1966) for the Lyman series and by Green et al. (1957) for the Balmer series.

The bound-free case requires special considerations. A discrete continuation of Kramers' formula into the domain of continuum frequencies is obtained through substitution of quantum number n with imaginary quantum number ik, where k is a real-valued integer:

$$n \rightarrow ik. \tag{34}$$

This is the reason for using the absolute value in Eq. (33), needed to preserve the positive sign of f.

$$f_{n'k} = G_{\rm II}\, f'_{n'k}, \tag{35}$$

where $G_{\rm II}$ is a second dimensionless Gaunt factor, also of order unity, given for instance in graphical form in Menzel & Pekeris (1935) and in greater detail by Karzas & Latter (1961). With the bound-bound resonant transition frequency given by

$$\omega_{nn'} = \omega_\infty\left[1-\left(\frac{n'}{n}\right)^2\right], \tag{36}$$

where ω_∞ is the frequency of the series limit ($n = \infty$), and the statistical weight $g_{n'} = 2n'^2$, Eqs. (32) and (33) become

$$f_{n'n} = \frac{2^5}{3\pi\sqrt{3}} \left(\frac{\omega_\infty}{\omega_{nn'}}\right)^3 \frac{n'}{n^3}\, G_{\rm I}. \tag{37}$$

Similarly,

$$\omega_{kn'} = \omega_\infty \left[1 + \left(\frac{n'}{k}\right)^2\right] \tag{38}$$

and

$$f_{n'k} = \frac{2^5}{3\pi\sqrt{3}} \left(\frac{\omega_\infty}{\omega_{kn'}}\right)^3 \frac{n'}{k^3}\, G_{\rm II}. \tag{39}$$

Note that we may in the following at any time switch our discussion from frequencies ω to wavelengths λ via a substitution of the type $\omega_\infty/\omega_{nn'} = \lambda_{nn'}/\lambda_\infty$.

To properly treat the bound-free contributions beyond the series limit (for $\lambda < \lambda_\infty$), we need to transform the discrete representation of Eq. (39) (in which k is an integer) into a continuous representation. Explicitly, the sum of ψ_e over the excited levels n_e in Eqs. (23) and (25) may be generalized to include not only the bound-bound but also the bound-free transitions by continuing the sum to go not only over $n = 1 \to \infty$, but also over $k = 1 \to \infty$. The bound-free sum $\sum_k \psi_e$ then needs to be transformed into an integral through the substitution

$$\sum_k \psi_e \to \int \psi_e \, {\rm d}k. \tag{40}$$

For simplicity we will here only do the bound-free calculations for the Rayleigh scattering case, since Raman scattering with $i \neq f$ does not contribute significantly to Lyman or Balmer scattering at visible wavelengths. In this case $\omega_{ei} = \omega_{ef}$, $\omega_f = \omega$, and since $\gamma \ll \omega_0$ can be disregarded in the dispersion wings,

$$\psi_e = 2g_i \frac{f_{n'k}}{\omega_{kn'}^2 - \omega^2} \tag{41}$$

according to Eq. (21). With Eqs. (35), (38)–(41), and the substitution $x = \omega_{kn'}/\omega$, we get

$$\int_0^\infty \psi_e \, {\rm d}k = \frac{g_i}{\omega^2} \frac{2^5}{3\pi\sqrt{3}} \frac{1}{n'} \left(\frac{\lambda}{\lambda_\infty}\right)^2 \times \int_{\lambda/\lambda_\infty}^\infty \frac{G_{\rm II}(x)\,{\rm d}x}{x^3(x+1)(x-1)}. \tag{42}$$

Since in the region beyond the series limit λ/λ_∞ is always <1, the integration range from λ/λ_∞ to infinity will include the pole $x = 1$. To the left of this pole the integral $\int_{\lambda/\lambda_\infty}^1 {\rm d}x$ diverges to $-\infty$, while to the right the integral $\int_1^\infty {\rm d}x$ diverges to $+\infty$. However, in a symmetric neighborhood ε of $x = 1$, if we replace x by $1+\varepsilon$, then for sufficiently small values of ε the integral in Eq. (42) when taken only over this neighborhood becomes, in the limit of vanishing ε,

$$\tfrac{1}{2} G_{\rm II}(1) \int_{-\varepsilon}^{+\varepsilon} \frac{{\rm d}\varepsilon}{\varepsilon} = 0. \tag{43}$$

The integral vanishes because $1/\varepsilon$ is an odd function. We may therefore solve the full integral numerically by splitting it in two parts, $\int_{\lambda/\lambda_\infty}^{1-\varepsilon} {\rm d}x$ and $\int_{1+\varepsilon}^\infty {\rm d}x$, where ε must be $\ll 1$, and the exclusion window must be placed fully symmetrically around the singularity. $G_{\rm II}(1) = 0.7973$ for $n' = 1$ (Lyman), 0.8762 for $n' = 2$ (Balmer) (Menzel & Pekeris 1935).

3.2. Lyman scattering opacity

As the $n' = 1$ state only consists of the $S_{1/2}$ state, the initial and final states i and f can only be different if the final state has $n \geq 2$. This is only possible for photons shortwards of Lyα, where the solar spectrum is orders of magnitude weaker than in the visible. For this reason only the Rayleigh scattering transitions $S_{1/2} \to P_{3/2} \to S_{1/2}$ and $S_{1/2} \to P_{1/2} \to S_{1/2}$ are of any practical relevance for scattering from $n' = 1$.

For Rayleigh scattering we have according to Eqs. (23) and (41)

$$\sigma = \frac{N}{\sum_{J_i} g_{J_i}} \sigma_e \sum_{J_e} \frac{3}{2J_e+1} \left| \sum_{n_e} \frac{g_i f_{ie}}{\left(\lambda/\lambda_{ei}\right)^2 - 1} \right|^2. \tag{44}$$

For the Lyman series, $g_i = \sum_{J_i} g_{J_i} = 2$, $J_e = 1/2$ and $3/2$, and the two oscillator strengths f_{ie} for the $S_{1/2} \to P_{1/2}$ and $S_{1/2} \to P_{3/2}$ transitions are 1/3 and 2/3 of the total oscillator strength $f_{n'n_e}$ for the transition $n' = 1 \to n_e$. This gives us the Lyman scattering cross section

$$\sigma_{\rm Ly} = N\sigma_e \left| \sum_{n_e} \frac{f_{1n_e}}{\left(\lambda/\lambda_{n_e 1}\right)^2 - 1} \right|^2, \tag{45}$$

where N is the total population of level $n' = 1$. For the principle of spectroscopic stability to be satisfied, we must retrieve the identical expression if we let the fine structure splitting go to zero, which is physically equivalent to letting the electron spin be zero and therefore have $J_e = L_e = 1$. In this case $g_i = \sum_{J_i} g_{J_i} = 1$, which, when inserted in Eq. (44), also leads to Eq. (45).

For the continuum range below the Lyman limit at $\lambda_\infty = 911.5$ Å, we need to replace the sum in Eq. (45) with the integral in Eq. (42) times $\omega^2/(2g_i)$ (cf. Eq. (41)).

The results for the scattering opacity $\sigma_{\rm Ly}$ per atom (i.e., for $N = 1$) are plotted in Fig. 2 over the wavelength range 0–3000 Å, in units of the Thomson scattering cross section σ_e. The dashed curve for wavelengths above the Lyman limit is a simple analytical approximation $\sigma_{\rm H}$ given by Baschek & Scholz (1982):

$$\sigma_{\rm H} = \sigma_e \left(\frac{966}{\lambda}\right)^4 \left[1 + \left(\frac{1566}{\lambda}\right)^2 + \left(\frac{1480}{\lambda}\right)^4\right], \tag{46}$$

where λ should be given in Å. We see from the figure that this approximation gives sufficient accuracy above 2000 Å.

To obtain well defined peak amplitudes for the bound-bound transitions, we have to choose the values for the Doppler widths and damping constants for the various bound-bound transitions. Here we have adopted a Doppler broadening of 2 km s^{-1} for all the resonances. The choice of damping constant for the Lyman lines will be defined in the context of a

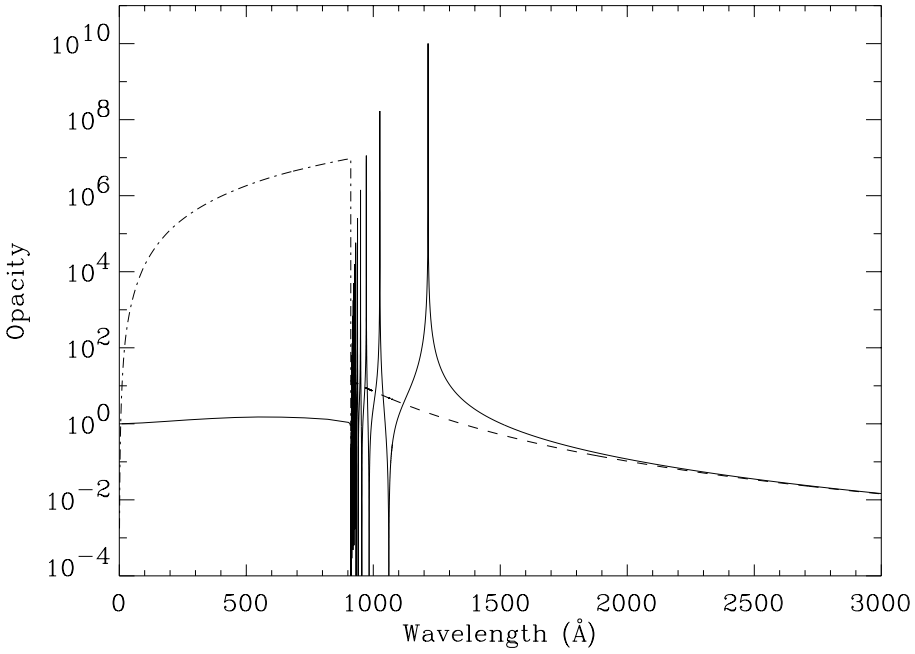

Fig. 2. Lyman scattering opacity per hydrogen atom, in units of the Thomson scattering cross section per electron. The dashed curve represents the analytic expression of Eq. (46), which is an excellent approximation above 2000 Å. Below the Lyman limit the scattering behaves as if the excited electron were free (like Thomson scattering), while the cross section for radiative ionization (dash-dotted curve) is many orders of magnitude larger.

discussion of the behavior of the Balmer bound-bound absorption near the series limit, which we will do in Sect. 3.6 below. The detailed pressure broadening mechanisms of the hydrogen lines are quite complex, but we do not need to go into these details here, since our focus is on the contributions to the continuum, which take place in the distant dispersion wings. The damping constant plays no role for the scattering opacity in the dispersion wings, as seen from Eqs. (44) and (45).

3.3. Bound-free absorption

Below the Lyman limit we have for comparison also plotted in Fig. 2 the coefficient for radiative ionization. According to Eq. (11) the total (integrated) contribution per atom from a discrete transition to the absorption coefficient is

$$\bar{\kappa}_{n'k} \,/\, N_{n'} \;= B_{n'k}\; h\nu/4\pi. \tag{47}$$

With Eq. (14) we get in terms of a continuum of states k,

$$\bar{\kappa}\; \mathrm{d}\nu \,/\, N_{n'} \;= \frac{e^2}{4\varepsilon_0\, m\, c}\; \mathrm{d}f_{n'k}, \tag{48}$$

where

$$\mathrm{d}f_{n'k} \;= f_{n'k}\, \mathrm{d}k = f_{n'k}\, \frac{\mathrm{d}k}{\mathrm{d}\nu}\; \mathrm{d}\nu. \tag{49}$$

From Eq. (38) we get

$$\frac{\mathrm{d}\nu}{\mathrm{d}k} \;= -\frac{2\nu_\infty\, n'^2}{k^3}, \tag{50}$$

which together with Eq. (39) gives

$$\bar{\kappa}_\nu\, \mathrm{d}\nu = 2.601\times 10^{-6} N\; \frac{G_{\mathrm{II}}}{n'}\; \left(\frac{\nu_\infty}{\nu}\right)^3\; \frac{\mathrm{d}\nu}{\nu_\infty} \tag{51}$$

(SI units), where N represents $N_{n'}$. For the Lyman transitions with $n' = 1$ and $\lambda_\infty = 911.5$ Å,

$$\bar{\kappa}_{\mathrm{Lyman}}(\nu) = 7.91\times 10^{-22}\, N\, G_{\mathrm{II}} \left(\frac{\lambda}{\lambda_\infty}\right)^3. \tag{52}$$

In units of the Thomson scattering cross section, which is

$$\sigma_e = 6.653\times 10^{-29}\ \mathrm{m}^2 \tag{53}$$

(cf. Eqs. (7) and (8)), the Lyman absorption per unit atom becomes

$$\frac{1}{N}\frac{\bar{\kappa}_{\mathrm{Lyman}}}{\sigma_e} = 1.189\times 10^7\, G_{\mathrm{II}} \left(\frac{\lambda}{\lambda_\infty}\right)^3, \tag{54}$$

which is about 7 orders of magnitude larger than the Lyman scattering cross section near the Lyman limit.

We see from Fig. 2 that the cross section for scattering via continuum states is almost identical to the Thomson scattering cross section at free electrons. This is to be expected, since when the continuum state is not a bound state, the electron will tend to behave like a free particle while in this state. It is also natural to expect the cross section for radiative ionization to be very much larger than the scattering cross section, since once the electron has become free, it is unlikely to return back to the initial state, as it would have to do in a scattering transition. The small likelihood that this will occur is automatically included in the present theory.

Another important feature that is the result of the coherent nature of the scattering process is the occurrence of very deep and narrow minima in the scattering opacity between the bound-bound resonant wavelengths. They are the result of quantum interference between the excited states of different n quantum number. We note in Eq. (45) that the scattering amplitude of each transition is negative for $\lambda < \lambda_{n_e 1}$ and positive for $\lambda > \lambda_{n_e 1}$. Between the resonances there is therefore cancellation between positive and negative contributions as the intermediate states are superposed coherently. It is because of these quantum cancellations that we get the deep, narrow dips in the scattering opacity. For the non-coherent process of radiative absorption, such dips do not occur (as we will see in Fig. 3 below).

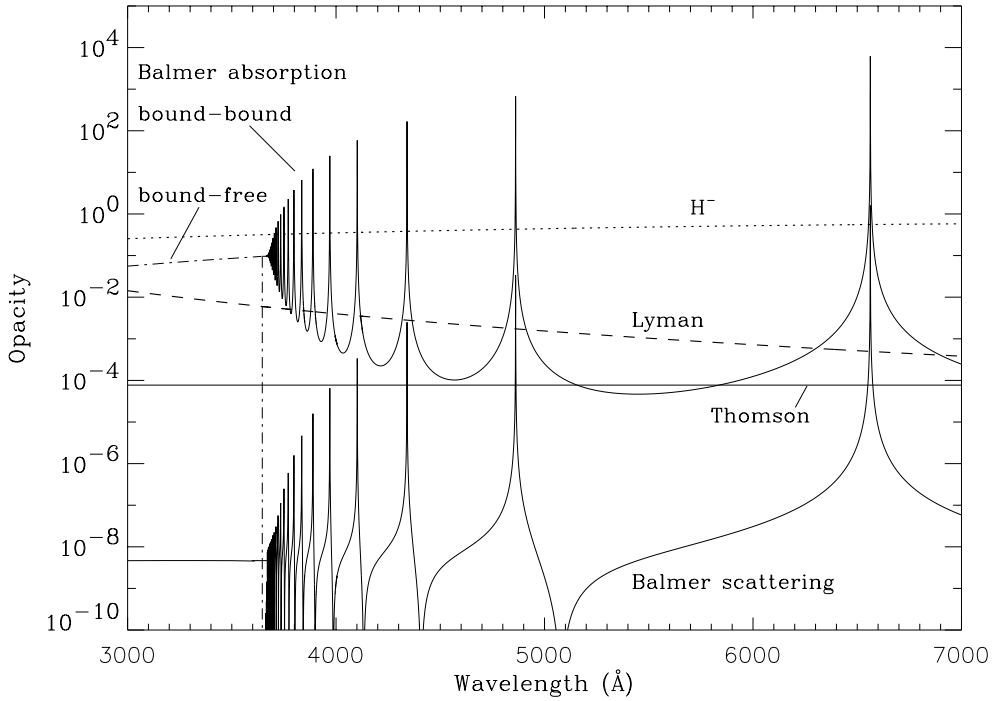

Fig. 3. Main contributors to the Sun's continuum opacity in the visible and near UV. The lower solid curve represents the Balmer scattering cross section, while the upper solid curve gives the cross section for bound-bound radiative absorption. Pressure broadening due to the statistical Stark effect is accounted for to describe convergence of the bound-bound opacities to the bound-free ones. Comparison is made with the Lyman scattering cross section (dashed), the Thomson scattering cross section (horizontal solid line), the H^- opacity (dotted), and the bound-free opacity for radiative ionization (dash-dotted). The relative contributions of these opacity sources depend on the electron densities and pressures and the relative level populations of hydrogen. The values chosen are typical for solar conditions.

3.4. Balmer scattering opacity

Only for a fraction of the emission processes in a Balmer line the excited state has been radiatively excited by that Balmer transition. Conversely, radiative absorption in a Balmer line is followed by Balmer emission in only a fraction of the cases. Therefore the Balmer scattering opacity is considerably smaller than the Balmer coefficient for radiative absorption. While this distinction is important for the Balmer case, it was not needed when considering Lyman scattering at visible wavelengths, since excitation from the ground state to a virtual state that lies far below the first resonance has no other decay channel than spontaneous emission back to the ground state, i.e., a Rayleigh scattering transition.

As we will see, the Balmer scattering opacity does not contribute significantly to the continuum polarization problem. The coefficient of bound-bound radiative absorption, on the other hand, becomes important as we get close to the Balmer series limit, across which it transforms itself from bound-bound to bound-free unpolarized opacity in a continuous manner, without any real discontinuity, because of the increasing collisional damping, which smears the resonances into a quasi-continuum near the series limit.

While the Lyman transitions have two fine-structure components, the Balmer transitions (with $n' = 2$) have 7: $S_{1/2} - P_{1/2}$, $S_{1/2} - P_{3/2}$, $P_{1/2} - S_{1/2}$, $P_{1/2} - D_{3/2}$, $P_{3/2} - S_{1/2}$, $P_{3/2} - D_{3/2}$, $P_{3/2} - D_{5/2}$, which can be combined to form Raman scattering transitions whenever $J_i \neq J_f$. Since the fine-structure splitting is small, we can for our continuum polarization problem neglect it by using the principle of spectroscopic stability and letting the electron spin be zero. In this simplified case, Balmer scattering can only occur in the form of three different Rayleigh scattering transitions, all of which have $i = f$: $S \rightarrow P \rightarrow S$, $P \rightarrow S \rightarrow P$, and $P \rightarrow D \rightarrow P$.

The application of the general theory to the Balmer case is done like in the Lyman case, although now we have to deal with the oscillator strengths of the individual fine structure components rather than with the total oscillator strength. In Fig. 3 we have plotted as the solid curve with the many resonances in the bottom part of the diagram the results for the Balmer scattering opacity per atom $\sigma_{\rm Balmer}$ in units of the Thomson scattering cross section, after scaling it with the Boltzmann factor $N_2/N_1 = 4\exp(-h\nu_{21}/kT)$, where ν_{21} is the frequency of Lyman α (since it defines the energy separation between the first two levels of hydrogen). Here we will use $T = 5740$ K (the Sun's effective temperature), which gives $N_2/N_1 = 4.62\times10^{-9}$. A more proper scaling would require radiative-transfer calculations, but for our order of magnitude comparison between the Balmer and Lyman opacity contributions, the exact choice is not important here.

As we see from a comparison with the Lyman contribution at visible wavelengths, obtained from expression (46) and plotted as the dashed curve in Fig. 3, the Balmer contributions to the continuum are at least 3 orders of magnitude smaller than the Lyman contributions, except in the vicinity of the Balmer resonant frequencies, where the Balmer contributions naturally dominate.

As in the case of Lyman scattering, the amplitudes of σ near the line cores are determined with the assumption that the Doppler broadening is 2 km s^{-1}, and that the damping constant varies as described in Sect. 3.6 below.

3.5. Bound-bound absorption

The coefficient for radiative absorption for bound-bound transitions $i \rightarrow e$ is given by Eq. (11). With Eq. (14) for B_{ie} and expressing the profile function in terms of a Voigt function $H(a, v)$, we obtain

$$\frac{\kappa_{ie}}{N_2} = 2.65 \times 10^{-6}\, f_{ie}\, \frac{2\,\omega_0}{\omega + \omega_0}\, \frac{1}{\Delta\nu_D\, \sqrt{\pi}}\, H(a, v) \qquad (55)$$

in units of m^2. N_2 is the population of the lower Balmer level (with $n' = 2$), and $\Delta\nu_D$ is the Doppler width. The factor $2\omega_0/(\omega + \omega_0)$ is needed to account for the non-resonant term of the profile function of Eq. (20).

Normalizing with the Thomson scattering cross section to make the expression dimensionless, multiplying with the relative level population factor N_2/N_1 to refer to the population N_1 of the ground state, and assuming a Doppler velocity of 2 km s^{-1}, we obtain

$$\frac{1}{N_1}\,\frac{\kappa_{ie}}{\sigma_e} = 10.4\, \frac{\lambda}{1 + \lambda_0/\lambda}\, f_{ie}\, H(a, v) \qquad (56)$$

if λ is expressed in Å. As for the scattering opacity it has been assumed that $N_2/N_1 = 4.62 \times 10^{-9}$.

The coefficient of radiative absorption as computed from Eq. (56) with the choice of damping constants as described in the next subsection is plotted in Fig. 3 as the solid resonant curve in the upper part of the diagram. Note how this curve does not have the deep dips between the resonances that the scattering opacity has, since these dips are exclusively due to quantum interferences, which only affect the scattering problem. When approaching the series limit the amplitude of the resonant oscillations of the curve goes to zero, which leads to a smooth and continuous transition to the coefficient for radiative ionization (bound-free case). The way in which the series limit is approached depends on the details of the pressure broadening of high-lying hydrogen levels and will be discussed in the next subsection.

For comparison we have in Fig. 3 also given the Thomson scattering cross section σ_T and the H$^-$ absorption coefficient σ_{H^-}. To obtain σ_T from σ_e we have applied as scaling factor an estimate of the ratio N_e/N_1 between the electron density and the hydrogen population density in its ground state. Based on model atmosphere calculations we adopt as a characteristic number $N_e/N_1 = 7.7 \times 10^{-5}$. We see that the Thomson scattering contribution to the continuum is 2–3 orders of magnitude larger than the Balmer scattering contribution, but typically one order of magnitude smaller than the Lyman contribution (with the difference decreasing with wavelength), and generally smaller than the Balmer bound-bound absorption coefficient, in particular as we approach the series limit.

Finally we make a comparison with the H$^-$ opacity, which we have taken from Chandrasekhar & Breen (1946), applied to an electron pressure of $P_e = 0.395$ (SI units) and a temperature of 5740 K. It has been plotted as the dotted curve in Fig. 3. H$^-$ is the dominating source of continuum opacity, typically two orders of magnitude larger than the Lyman contribution.

3.6. Shift and smoothing of the Balmer jump

The level of the scattering opacity outside the immediate cores of the resonances is independent of the assumption for the damping constant γ, as seen from Eqs. (23) and (21). In contrast, for the coefficient of bound-bound radiative absorption the levels of the distant line wings scale with γ, as seen from Eqs. (11) and (16). Note also that the wings of the Voigt profile $H(a, v)$ in Eq. (56) scale with γ. The coefficient for bound-bound absorption is therefore a sensitive function of the line-broadening processes. Doppler broadening affects only the line cores and is unimportant in the wings, where collisional or pressure broadening dominate.

Pressure broadening increases greatly as we approach the series limit. This smearing leads to a merging of the crowded high-level resonances into a quasi-continuum before the ionization limit is reached, resulting in a gradual approach to the ionization limit rather than a discontinuous jump. It is beyond the scope of the present paper to model in any quantitative detail how this quasi-continuum is formed. The aim here is to try to clarify the main physics involved and make a relatively crude approximate treatment that can be used to compare with the observations and thereby to verify that the relevant physical mechanisms have been identified.

Pressure broadening of the hydrogen lines is normally described in terms of the statistical Holtsmark theory, according to which the broadening is due to the Stark effect splitting of the lines from the statistically fluctuating electric fields of the surrounding ions and electrons. The resulting Holtsmark shape of the absorption coefficient in the line wings is found to vary with $1/\Delta\lambda^{5/2}$ (Unsöld 1955). As this is steeper than the $1/\Delta\lambda^2$ decrease of the unbroadened, quantum-mechanical dispersion wings, the ordinary opacity from the dispersion wings will take over at large distances from the resonances. Since for the continuum problem we are only interested in the behavior far from the resonances, it is a reasonable approximation for our purposes to describe the lines in terms of Voigt profiles with a damping constant γ, which leads to a $1/\Delta\lambda^2$ behavior in the wings. For γ we use

$$\gamma = \Delta E/\hbar, \qquad (57)$$

where ΔE is the typical splitting due to the Stark effect.

Following Inglis & Teller (1939) and Unsöld (1955),

$$\Delta E \approx \frac{3}{2}\, a\, e\, F \qquad (58)$$

for the outer components of the Stark splitting pattern, where e is the electron charge, F the electric field strength, and a the major half-axis of the electron orbit around the nucleus.

$$a = a_0\, n^2, \qquad (59)$$

where n is the main quantum number, and

$$a_0 = 5.29 \times 10^{-11}\ \text{m} \qquad (60)$$

is the Bohr radius. Since the energy separation between the excited states decreases as $1/n^3$ as we approach the series limit, while the Stark splitting goes as n^2, we see that the splitting must become larger than the level separation above a certain level n. This is where the quasi-continuum begins. It is approached in a continuous manner when going to shorter wavelengths.

According to Unsöld (1955),

$$F = 8.8\, e\, N^{2/3} \tag{61}$$

in cgs units, where N is the number density of charged particles (ions and electrons). Different authors give different values for the numerical factor, but such differences are irrelevant for our approximate treatment. As an exception we give here the numerical factor in cgs rather than SI units, to allow direct comparison with previous literature.

The damping parameter a in the Voigt function is $\gamma/(2\Delta\omega_{\rm D})$, or, using the Doppler formula,

$$a = \frac{\gamma\,\lambda}{4\pi\, v_{\rm D}}. \tag{62}$$

Choosing $v_{\rm D} = 2\ {\rm km\,s^{-1}}$ for the Doppler velocity and $N = 10^{19}\, m^{-3}$ for the particle number density as typical values for the solar atmosphere, we obtain from Eqs. (57)−(62)

$$a = 3\times 10^{-5}\, n^2\, \lambda\,({\rm Å}). \tag{63}$$

Using this expression in Eq. (56), we obtain the upper resonant curve that represents bound-bound absorption in Fig. 3. The reason why the oscillation amplitude of the resonances goes to zero so quickly as we approach the series limit is that the pressure broadening due to the Stark effect increases to become larger than the level separation. Without this effect the oscillation amplitudes would stay large much closer to the series limit.

In the range below the Balmer limit we plot in Fig. 3 as dot-dashed the bound-free cross section for radiative ionization, like in Fig. 2. We see that this bound-free cross section is reached well before the series limit by the rapid convergence of the bound-bound cross section oscillations. We also note that the Balmer absorption opacity becomes comparable to the H^- opacity near the Balmer limit and is larger there than the Lyman scattering opacity (dashed line in Fig. 3). The wavelength where the bound-bound radiative absorption coefficient surpasses the Lyman opacity lies approximately 140 Å above the series limit and is the place where the effective "Balmer jump" transition in the scattering polarization may be expected to begin. A wavelength shift of order 100 Å of the apparent Balmer jump is indeed seen in the observational data, as we will see below.

In the present simplified treatment we have not accounted for collisional ionization, which increases with n, and photoionization, which decreases with n. For high levels collisional ionization will dominate over bound-bound radiative absorption and couple effectively to the continuum state. This may speed up the transition to a quasi-continuum and thereby both shift and steepen the effective Balmer jump. The quantitative details of this complex subject is however outside the scope of the present paper.

3.7. Effective polarizability

As we have seen in Sect. 2.4, the intrinsic polarizabilities $W_2 = \sigma_2/\sigma_0$ of the individual scattering transitions need to be combined, weighted according to their relative opacity contributions, to obtain the effective polarizability $W_{2,\,\rm eff}$ of the medium. With

$$\sigma_{\rm tot} = \sum_j \sigma_j, \tag{64}$$

where $\sigma_j = \sigma_{0,j}$ are the different opacities, we can write Eq. (27) as

$$W_{2,\,\rm eff} = \sum_j \frac{\sigma_j}{\sigma_{\rm tot}}\, W_{2,j}. \tag{65}$$

In the case of the continuum polarization of the visible solar spectrum, we have seen from Fig. 3 that there are only four opacity contributions of any practical relevance for the continuum: Two of them, H^- (σ_{H^-}) and Balmer radiative absorption $\sigma_{\rm Balmer}$ (bound-bound above, bound-free below the Balmer limit), have polarizability zero, while the other two, Lyman ($\sigma_{\rm Lyman}$) and Thomson ($\sigma_{\rm Thomson}$) scattering, have polarizability unity (like classical dipole scattering). The polarizability of Balmer scattering is more complicated and of intermediate magnitude, since the three contributing fine-structure scattering transitions have different polarizabilities and need to be weighted together properly. Since however the Balmer scattering opacity is insignificant in the continuum polarization context, we will not address this problem further here.

A more correct way to add the opacity contributions in a weighted way is to attach $\int \varphi_\nu J_\nu\, {\rm d}\nu$ to the scattering transitions, and $B_\nu(T)$ to the pure absorption transitions if they are treated in LTE. This kind of weighting is automatically done in the formalism of radiative transfer. Here, in our phenomenological treatment that bypasses radiative transfer, we make the simplifying LTE-type assumption that $\int \varphi_\nu J_\nu\, {\rm d}\nu$ and B_ν are of the same magnitude, which allows us to simply write

$$\sigma_{\rm tot} = \sigma_{\rm Lyman} + \sigma_{\rm Thomson} + \sigma_{H^-} + \sigma_{\rm Balmer}. \tag{66}$$

Then

$$W_{2,\,\rm eff} = \frac{\sigma_{\rm Lyman} + \sigma_{\rm Thomson}}{\sigma_{\rm tot}}. \tag{67}$$

The way in which the relative contribution of $\sigma_{\rm Balmer}$ to $\sigma_{\rm tot}$ varies as the bound-bound opacity contributions converge to the bound-free ones governs the shape and magnitude of the effective Balmer jump in the effective polarizability $W_{2,\,\rm eff}$ and the observed polarization, as we will see below in Sect. 4.3.

4. Empirical determination of the continuum polarization

We base our empirical determination of the continuum polarization on the Atlas of the Second Solar Spectrum that has been compiled in three voumes by Achim Gandorfer. Atlas

Vol. I covers 4625–6995 Å (Gandorfer 2000), Vol. II covers 3910–4630 Å (Gandorfer 2002), while the still unpublished Vol. III covers 3161–3913 Å. The scattering polarization (Stokes Q/I) in the solar spectrum has been recorded in seemingly non-magnetic solar regions near the limb, always at a limb distance that corresponds to $\mu = 0.1$ (which is 5 arcsec inside the extreme limb). The positive Q direction is defined as the direction parallel to the nearest solar limb, i.e., perpendicular to the radius vector from disk center. All the recordings have been made with the Zurich Imaging Polarimeter ZIMPOL (cf. Povel 1995). For Volumes I and II of the Atlas ZIMPOL was used at IRSOL (Istituto Ricerche Solari Locarno), for Vol. III that covers the UV portion ZIMPOL was used at the McMath-Pierce facility of the National Solar Observatory (Kitt Peak).

While the three atlases provide very high accuracy in terms of relative polarization values, the zero point of the polarization scale cannot be determined with comparable precision due to instrumental effects. On spectral scales less than about 10 Å the relative spectral variations in Q/I with the polarized line profiles are very well determined, but the Q/I zero-point offset is floating around on spectral scales larger than 10 Å. In the published atlases the Q/I zero point has been fixed by fitting the polarized continuum to the theoretical value derived from the radiative-transfer theory of Fluri & Stenflo (1999). This procedure of relying on theory however cannot be used if we want to obtain an empirical determination of the continuum polarization from the atlas data. For such a determination we have to regard the zero point of the polarization scale as an entirely unknown quantity that needs to be determined in the same context together with the value for the continuum polarization. The adopted procedure for doing this will be outlined in the next subsection.

4.1. Depolarizing blend lines and the zero point of the polarization scale

The richly structured Second Solar Spectrum contains, like the ordinary intensity spectrum, a multitude of spectral lines superposed on a background continuum. In the polarized spectrum we can distinguish between two types of lines: depolarizing and intrinsically polarizing lines. For the depolarizing lines the unpolarized line opacity dilutes the polarizing continuum opacity such that the continuum polarization level gets depressed. In Q/I such lines therefore have the appearance of absorption lines, similar to the corresponding absorption lines in the intensity spectrum. The intrinsically polarizing lines, on the other hand, appear like "emission" lines in Q/I if they polarize more than the continuum. The Second Solar Spectrum contains a mixture of both types of lines. Since the amount of intrinsic line polarization is modified by the Hanle effect through the presence of hidden, turbulent magnetic fields (Stenflo 1982), and since these fields vary with time, the relative proportion of absorption- and emission-like lines in the Second Solar Spectrum varies with phase of the solar cycle (cf. Berdyugina et al. 2002).

Let us assume that we have been able to find a spectral region that only contains purely depolarizing lines that have no intrinsic line polarization. Let $p = Q/I$ be the "true" polarization (without zero-point error) and p_c the corresponding level of the continuum (outside the spectral lines). Then we may model the relative line depth in Q/I in terms of the relative line depth in intensity I with the following one-parameter model:

$$\frac{p_c - p}{p_c} = \left(\frac{I_c - I}{I_c}\right)^{\alpha} . \tag{68}$$

Here I_c is the continuum intensity, and α is the free model parameter that determines the shape of the depolarizing lines. For $\alpha = 1$ the relative line depths in Stokes I and Q/I would be identical. For smaller values of α the relative Q/I line depth is larger than the I line depth. In the extreme case of $\alpha = 0$ even minor depressions in intensity would result in complete depolarization, which is certainly not observed.

While a statistical analysis of the first atlas survey of the Second Solar Spectrum (based on observations made in 1978, in Stenflo et al. 1983a,b) suggested that a value of $\alpha = 1$ would provide an adequate description of the depolarizing lines, later work with ZIMPOL indicated that a considerably lower value, like $\alpha = 0.55$, would be more appropriate for the particular spectral windows that were considered (Stenflo et al. 1998). More recently the theoretical mechanisms behind the formation of the depolarizing line profiles have been identified, and a parameter survey has been performed (Fluri & Stenflo 2003). It is found that the depolarizing line depth is a sensitive function of height of formation, and that this function is entirely different for lines formed by pure absorption as compared with lines formed by unpolarized scattering. In terms of the simplified model of Eq. (68), one may say that the value of the parameter α depends on the details of line formation and may vary considerably from one line to the other. Theory does not allow us to find a value of α that applies to *all* lines, there will be a substantial scatter between the lines. Therefore Eq. (68) only has validity in a statistical sense for an ensemble of spectral lines, and it is prudent to treat α as a free parameter that is poorly known.

Since the zero point of the polarization scale is unknown and floating around on scales larger than 10 Å, the observed polarization p_{obs} is the sum of the true polarization p and the value p_0 of the true zero point on the chosen polarization scale:

$$p_{obs} = p + p_0. \tag{69}$$

The measured intensities I are usually normalized to some maximum intensity value I_{max} in the observed spectral windows. This produces a dimensionless observed quantity b_{obs}, but the value of I_{max} may differ from the true continuum by a factor f. Thus

$$\begin{aligned} b_{obs} &= I/I_{max}, \\ I_c &= f I_{max}. \end{aligned} \tag{70}$$

Combining Eqs. (68)–(70) we obtain

$$p_{obs} = p_c \, [\, 1 - (1 - b_{obs}/f)^{\alpha} \,] + p_0. \tag{71}$$

p_{obs} and b_{obs} are the observables that are obtained from the atlases as functions of wavelength, while p_c, p_0, α, and f are the four model parameters.

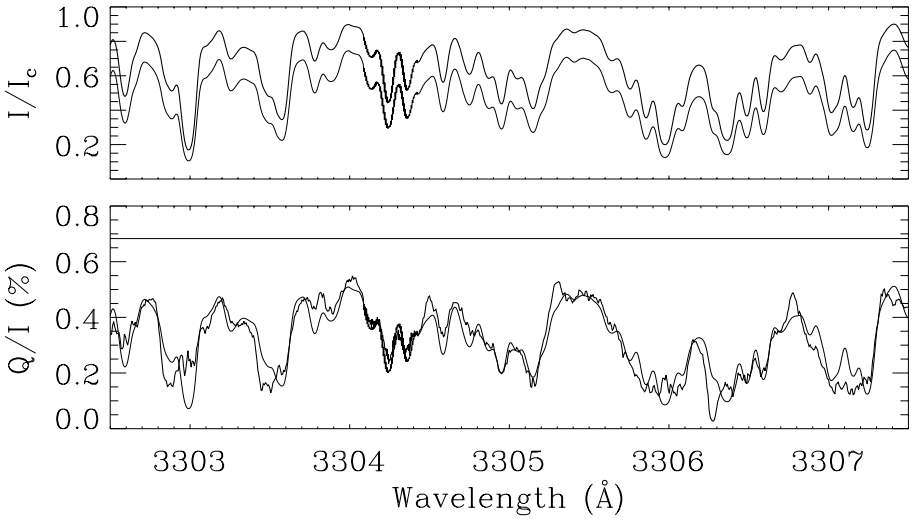

Fig. 4. Illustration of a 2-parameter fit to the observed Q/I with the model given by Eq. (71), assuming that $\alpha = 0.6$. The thick solid lines represent the observations (taken from the currently unpublished UV portion of Gandorfer's Atlas of the Second Solar Spectrum), while the thin curves represent the model. The determined level of the continuum polarization p_c is given by the horizontal line in the bottom panel.

The parameter f only presents a certain problem in the UV, where the spectrum is very crowded, and no clean continuum window is available. Here the level of the intensity continuum I_c is chosen manually to be consistent with other spectral atlases. This choice of I_c fixes the value of parameter f and leaves us with three free model parameters, which can be determined by an iterative least squares fitting method. Although such a 3-parameter fit generally converges to a unique solution, the goodness of the fit depends only weakly on parameter α. The fit procedure becomes numerically much more robust if we fix the value of α and only seek to determine the two free parameters p_c (the continuum polarization) and p_0 (the zero point of the polarization scale).

The procedure is illustrated in Fig. 4, where we for clarity have selected a spectral region that seems to be devoid of intrinsically polarizing lines. The thick solid lines represent the observations, while the thin solid lines illustrate the model. In this example we have assumed ad hoc that the value of α is 0.6, and then done a 2-parameter fit to the observed Q/I curve. The so obtained value p_c of the continuum polarization is given as the horizontal line in the lower panel (Q/I). The thin curve in the upper panel (I/I_c) represents $[(I_c - I)/I_c]^{0.6}$. This curve, when scaled with the value of p_c, becomes the thin fit curve in the lower panel. We see that the fit is excellent, which means that the value of p_c is very accurately determined, provided that the value of α has been chosen correctly.

Note that the thick solid curves are slightly thicker around 3304.3 Å, since there is the overlap region of two separate spectral recordings that have been pieced together to cover the whole spectral window shown in Fig. 4. The almost imperceptible broadening of the curves in the overlap region illustrates the nearly perfect reproducibility of every single wiggle of the spectral recordings in both I/I_c and Q/I, which indicates that practically all the tiny Q/I wiggles are solar features and not noise.

The excellent match that we see between the thick and thin curves in the Q/I diagram would be nearly as perfect also for other values of α, so the quality of the fit cannot be used as a good criterion for the selection of α. The only significant change in the fit diagram is that the Q/I continuum level and zero point would be placed differently for other values of α. With the help of Fig. 4 we can however understand and get a feeling for how the extracted value of p_c depends on α. If α were larger, for instance unity, the thick and thin curves in the I/I_c panel would coincide. This would in the Q/I diagram have the effect both that the continuum level would be lowered to lie closer to the observed curve, and at the same time that the zero point of the scale would be lowered as well to be somewhat farther from the observed curve. These effects partly compensate each other in producing a value for p_c, but for the special case of Fig. 4 the lowering of the continuum is somewhat larger than the lowering of the zero point, so that the net effect is a reduction of p_c. This net effect is however relatively small.

In spectral regions with little line blanketing and weak absorption lines, however, which is the situation in the red part of the spectrum, an increase of α from 0.6 to 1.0 will have the opposite net effect: The zero level will be lowered more than the continuum level, so that the value of p_c will increase with increasing α. In summary we see that the dependence of the extracted value of p_c on the assumed value of α is opposite between the UV and the red parts of the spectrum, since it is related to the degree of line blanketing, but that on average the dependence is relatively modest. This rather weak dependence on α implies that our method of finding the empirical value of the continuum polarization should be rather robust in spite of the uncertainties in our knowledge about the formation of the depolarizing lines.

4.2. Results of model fitting

We have seen in the preceding subsection that the fit procedure works well, provided that the spectral fit region exclusively contains depolarizing lines. The spectral region in Fig. 4 with only depolarizing lines that we have used to illustrate the method is however not typical for the Second Solar Spectrum. Usually, intrinsically polarizing lines are abundant everywhere in the spectrum. Their presence would invalidate the model fit, since the model is based on Eq. (68), which of course has no validity for lines with intrinsic polarization. We therefore have

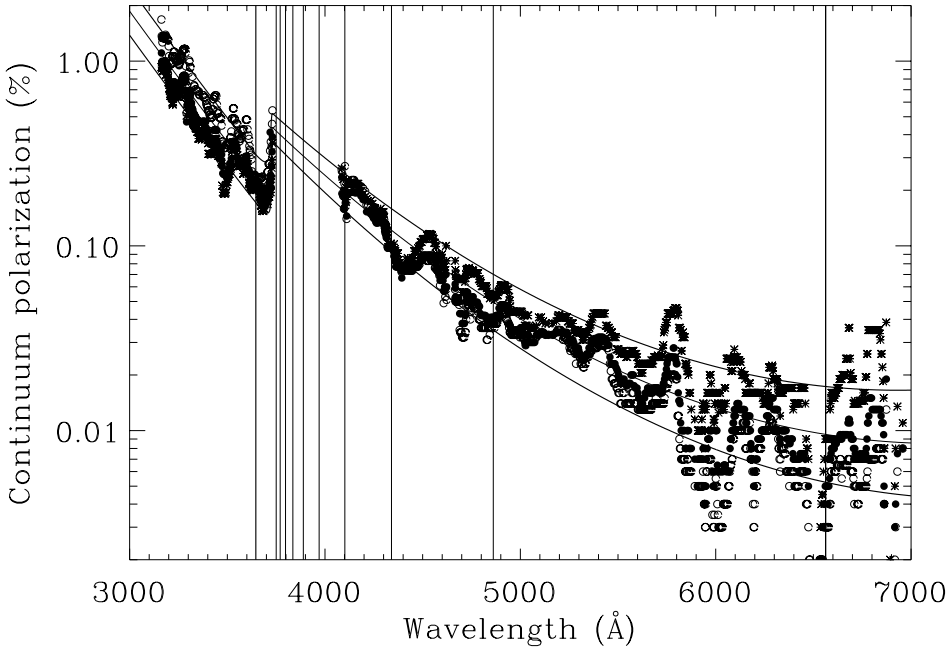

Fig. 5. Continuum polarization p_c, as determined from the Atlas of the Second Solar Spectrum using the model of Eq. (68). Asterisks represent model fits with $\alpha = 1.0$, filled circles fits with $\alpha = 0.6$, open circles fits with $\alpha = 0.3$. The vertical lines give the resonance wavelengths of the first ten Balmer lines, plus the series limit as the left-most vertical line. The three solid curves represent second-order polynomial fits to the $\log p_c$ values: a central curve as the most likely representation, and two outer curves that indicate the approximate lower and upper limits.

to take great care to exclude intrinsically polarizing lines before applying the fit procedure.

Intrinsic line polarization comes with all kinds of amplitudes and profile shapes and is therefore difficult to identify and isolate except in the cases when the line polarization clearly dominates over the continuum polarization with profile features that look like "emission" lines in Q/I. Due to the highly individualistic behavior of the spectral features in the Second Solar Spectrum we have refrained from trying to find some automated computer algorithm that could decide whether or not intrinsic line polarization is present at a given wavelength, and instead resorted to a manual procedure. Thus we have done careful visual inspection of the Second Solar Spectrum with educated judgement based on many years of experience in dealing with this spectrum, and so defined hundreds of "exclusion windows" of various widths throughout the spectrum. The data inside these exclusion windows are skipped by the least squares fit procedure because of their "contamination" with intrinsic line polarization.

To determine the continuum polarization p_c as a function of wavelength we divide the spectrum into a sequence of partially overlapping segments. Each segment consists of approximately 660 points, with the wavelength monotonically increasing but with the exclusion windows skipped. If no exclusion window is present, 660 points corresponds to about 6 Å, otherwise the segment as expressed in Å is wider. For each segment p_c and p_0 are determined by the iterative least squares fit, using widely different start values for the iterations to verify the uniqueness of the fit. Due to the uncertainty in the proper choice of α to use for the fit, we make three sets of fits throughout the whole spectrum, for the three widely different α values 0.3, 0.6, and 1.0. It is highly unlikely that the statistically "true" value of α would lie outside this very wide range. Trials with 3-parameter fits, using α as a free parameter, result in a wide distribution of α values, but the bulk of the distribution is bracketed by the extreme values of $\alpha = 0.3$ and 1.0 that we have chosen here.

The results of these fits are presented in Fig. 5, where the p_c values for each spectral segment are plotted (in logarithmic scale) vs. the average wavelength of the segment. Three different symbols are used for the three α values: asterisks for $\alpha = 1.0$, filled circles for $\alpha = 0.6$, and open circles for $\alpha = 0.3$. To reduce the scatter of the points we have in Fig. 5 applied median smoothing with a running window that increases in width from 11 segments in the UV to 21 segments in the red. The corresponding window width in Å depends on the distribution of the exclusion windows but is of order 100 Å in the UV and 200 Å in the red. This is smaller than the scale over which p_c varies significantly.

We notice a big gap in the data points between 3730 and 4090 Å. The reason for this is not the absence of data but the circumstance that this region is completely swamped with strongly polarizing lines, which invalidate our procedure to find the continuum polarization. The polarization from the Ca II K 3933 and H 3968 Å lines dominates the spectrum over more than 200 Å. In the lower portion of the gap the spectrum is crowded with polarizing lines of the CN molecule as well as a number of strong iron lines, while in the upper portion of the gap there are some very strongly polarizing lines of Fe I and Sr II.

For reference, vertical lines have been drawn in Fig. 5 to mark the location of the Balmer series lines (up to H_{10}) as well as the Balmer limit at 3646 Å (the left-most vertical line). The most notable feature here is a very clear and conspicuous Balmer jump, which however does not occur at the series limit but at considerably longer wavelengths (nearly 80 Å longer), as expected from pressure broadening of the highly excited hydrogen levels, as explained in Sect. 3.6.

We notice in Fig. 5 a slight but systematic dependence of the fit values on the assumed value of parameter α. At longer wavelengths the asterisks lie systematically above the open

circles, while in the UV the opposite situation is the case. An explanation for this wavelength variation of the α dependence was given at the end of the preceding subsection.

In the UV the main source of scatter of the points is due to the systematic α dependence of the results. At higher wavelengths, however, other sources of scatter dominate, much because of the presence of non-excluded lines with weak and inconspicuous intrinsic polarization. Figure 5 may give the misleading impression that the noise gets larger with increasing wavelength. However, we have to remember that the polarization in the figure is given with a logarithmic scale, and that the amplitude decreases by two orders of magnitude, from about 1% to about 0.01%, as we go from the UV to the red part of the spectrum. It is actually remarkable that it is at all possible to extract the minute values of the continuum polarization from the atlas data at these long wavelengths. That this can be done is testimony to the high quality of the atlas data.

In the following we will not try to distinguish between the various sources of scatter of the data points. Thus we will not try to treat the data referring to the three different symbols differently, but will consider the scatter of all the symbols as representative of the uncertainty in the determination of the continuum polarization p_c. Since we know from theory that p_c is expected to vary only slowly with wavelength (except near the Balmer jump) in a lin-log representation like Fig. 5, it is sufficient to describe the dependence of $\log p_c$ on wavelength in terms of a second-order polynomial. However, because of the Balmer jump, we have to use a different second-order polynomial below and above the Balmer jump, as well as a special, steep polynomial in the region 3650–3730 Å where the Balmer jump is found to take place.

Because of the large scatter of the $\log p_c$ values we should not attach significance to the rapid fluctuations of the data points, like to the apparent peak near 5800 Å, since these fluctuations are most likely due to the statistical nature of the extraction method used and to ubiquitous contamination from intrinsically polarizing spectral lines. Instead we have found it convenient to do smoothing by choosing second-order polynomials by hand (rather than by automated fits). Three such sets of curves have been selected and are shown in Fig. 5. The two outer curves represent what we consider to be the approximate lower and upper limits to the empirical values of p_c, between which the bulk of the data points fall, while the central curve is exactly in the middle between the two limit curves and represents our best estimate for p_c. Theoretical modelling should aim at reproducing the middle curve, within the tolerance region defined by the outer curves.

4.3. Comparison with theory

At the time when the radiative-transfer theory for the formation of the continuum polarization was developed (Fluri & Stenflo 1999), there did not exist adequate empirical data with which the theoretical values could be compared in a meaningful way. However, now we are in a position to make such a comparison. In Fig. 6 the empirically allowed region, defined as the region between the outer polynomial curves in Fig. 5, is given as the shaded area. The solution of the polarized transfer equation with a numerically given model atmosphere, as obtained by Fluri & Stenflo (1999), is shown by the dashed curve. This radiative-transfer theory has only been applied above 4000 Å and therefore does not address the interesting region around the Balmer jump.

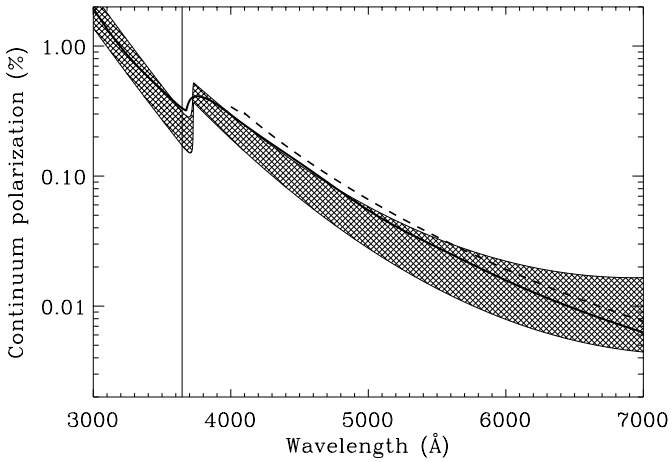

Fig. 6. Comparison between observations and theory. The shaded area represents the empirically allowed region, defined as the region between the two outer polynomial curves in Fig. 5. The vertical line marks the wavelength of the Balmer series limit. The dashed curve has been obtained from the radiative-transfer theory of Fluri & Stenflo (1999). The thick, solid curve is based on the last scattering approximation, Eq. (72), with the anisotropy and the opacities given by Figs. 1 and 3. Note in particular the large displacement of the Balmer jump with respect to the series limit.

Although the empirical and theoretical curves behave in similar ways, it is notable that the dashed curve lies systematically above the empirically allowed region for wavelengths below about 5700 Å. Although the source of this discrepancy cannot be identified at the present time, it is likely to be related to the choice of model atmosphere. The radiative-transfer problem needs to be revisited, both to extend the theory to shorter wavelengths and to fit the empirical data by modifying the model atmosphere. Our continuum polarization data may serve as a qualitatively new type of constraint on models of the solar atmosphere.

For comparison, the thick, solid curve in Fig. 6 represents the values for p_c that we get when we bypass radiative-transfer theory and use the last scattering approximation as explained in Sect. 2.5. What is plotted is simply

$$p_{c,\,\text{last scatt.}} = k_G\ W_{2,\,\text{eff}}. \tag{72}$$

For the anisotropy factor k_G we use the values that were given in Fig. 1, while for the intrinsic polarizability we use Eq. (67) with the opacities exactly as given by Fig. 3, but with the following special considerations for the Balmer opacity σ_{Balmer} that contributes to the total, unpolarized opacity σ_{tot} in Eqs. (66) and (67): for the continuum problem we are not interested in the opacity near the line cores but only in the wing opacity between the resonances. Therefore we have for the bound-bound contributions to σ_{Balmer} used a smooth lower envelope to the oscillating radiative absorption curve of Fig. 3

to filter out the resonant contributions. Since this lower envelope increases steeply as we approach the series limit, overtaking the Lyman scattering contribution and becoming comparable in magnitude to the H^- contribution, it governs the behavior of the effective Balmer jump in Fig. 6.

The shape and position of the Balmer jump in $p_{c,\,\text{last scatt.}}$ in Fig. 6 appear similar to the Balmer jump in Fig. 1 of the anisotropy factor k_G alone. Since $p_{c,\,\text{last scatt.}}$ represents the product of k_G and $W_{2,\,\text{eff}}$, the question arises which of these two factors is most responsible for the Balmer jump in Fig. 6. To answer this question we have replaced k_G in Eq. (72) with a straight, slanted line without any Balmer jump. The influence on the shape and magnitude of the Balmer jump in $p_{c,\,\text{last scatt.}}$ is insignificant. If we remove the bound-bound Balmer opacity contributions, the Balmer jump appears as a sharp discontinuity exactly at the location of the series limit, regardless of whether we remove or retain the observed Balmer jump in Fig. 1 from k_G. These tests conclusively show that the Balmer jump in Fig. 6 comes almost exclusively from a corresponding Balmer jump in $W_{2,\,\text{eff}}$, while the influence of the Balmer jump in k_G on $p_{c,\,\text{last scatt.}}$ is a second-order effect that plays a subordinate role.

The similarity of the Balmer jumps in $W_{2,\,\text{eff}}$ and k_G points to a common origin: the wavelength variation of $\sigma_{\text{Balmer}}/\sigma_{\text{tot}}$. This ratio becomes significant already at considerably longer wavelengths than the formal Balmer limit. Due to the increasing pressure broadening the bound-bound opacity converges to the bound-free opacity long before the series limit is reached.

It is to be noted that the empirically determined Balmer jump appears to be more abrupt and discontinuous than can be accounted for by our simplified theory, as seen from Figs. 5 and 6. The observed shape of the Balmer jump may therefore serve as a constraint on refined theories for the pressure broadening of atomic energy levels in stellar atmospheres. Unfortunately it is difficult to determine the detailed shape of the Balmer jump from polarimetric observations, since it occurs near the edge of the excluded region in Fig. 5, which is filled with intrinsically polarizing lines.

4.4. Center-to-limb variation

Through model fitting of the data in the Atlas of the Second Solar Spectrum we have obtained the function p_{emp} that represents the continuum polarization at the particular center-to-limb distance that is defined by $\mu = 0.1$ (where μ is the cosine of the heliocentric angle). To connect this result to other μ values we need the help of radiative-transfer calculations that have established the relative shape of the center-to-limb variations.

According to the radiative-transfer theory of Fluri & Stenflo (1999) the results of the numerical calculations can be closely approximated by the following semi-analytical formula for the continuum polarization $p_c(\mu)$ as a function of μ and of wavelength λ:

$$p_c(\mu) = q_\lambda\, f_\lambda(\mu), \tag{73}$$

where q_λ is a function of wavelength only, while the μ dependence is contained in

$$f_\lambda(\mu) = \frac{1-\mu^2}{(\mu + m_\lambda)\, I_\lambda(\mu)/I_\lambda(1.0)}. \tag{74}$$

$I_\lambda(\mu)/I_\lambda(1.0)$ represents the center-to-limb variation of the intensity, for which we will use an anlytical fit to the empirical results of Neckel (1996), which represents a somewhat more sophisticated representation than the one given by Eq. (30). The parameter m_λ has a slow wavelength dependence, which for the range 4000–8000 Å (for which the radiative-transfer calculations have been performed) can be represented by the linear function

$$m_\lambda = b_0 + b_1\,\lambda, \tag{75}$$

with the coefficient values $b_0 = 0.14$ and $b_1 = -1.6\times10^{-5}$ (if λ is given in Å). m_λ thus increases from 0.028 at $\lambda = 7000$ Å to 0.076 at 4000 Å. Since we have no guidance from radiative transfer below 4000 Å, and extrapolation of Eq. (75) to shorter wavelengths would lead to suspiciously high values for m_λ, we have adopted the value 0.076 as the most reasonable choice for all wavelengths below 4000 Å. Note, however, that errors in m_λ only affect the center-to-limb variation near the extreme limb, for $\mu \lesssim 0.1$, while the rest of the curve remains robust.

Expressed in terms of the above functions, our empirically determined continuum polarization $p_{\text{emp}} = p_c(0.1)$ becomes

$$p_{\text{emp}} = q_\lambda\, f_\lambda(0.1). \tag{76}$$

Combined with Eq. (73) we can eliminate q_λ and so obtain the continuum polarization p_c for all μ and λ as

$$p_c(\mu) = p_{\text{emp}}(\lambda)\, f_\lambda(\mu)/f_\lambda(0.1). \tag{77}$$

As our best empirical determination of $p_{\text{emp}}(\lambda)$ we use the central polynomial curve from Fig. 5. This curve is plotted in the two upper panels of Fig. 7, both with a logarithmic and a linear scale for p_c. The abrupt and wavelength-shifted Balmer jump is conspicuous in these plots. It is also striking from the linear plot how miniscule the continuum polarization becomes above 6000 Å. It is remarkable that it could at all be determined with reasonable error bars in this region.

The two lower panels in Fig. 7 show the center-to-limb variation of the continuum polarization for $\lambda = 4000$ Å, both with a logarithmic and a linear scale for p_c. They illustrate the steepness of the center-to-limb variation, whose shape is given by function $f_\lambda(\mu)$ of Eq. (74).

5. Conclusions

A number of different physical processes contribute to the formation of the polarized continuum at visible wavelengths. With the exception of Thomson scattering at free electrons they all have to do with absorption or scattering by hydrogen. The only processes that contribute with polarized photons are Lyman scattering at hydrogen in its ground state and Thomson scattering. Lyman scattering is the larger of the two, although the scattering takes place so far from the Lyman resonances. The polarized photons get diluted by the unpolarized

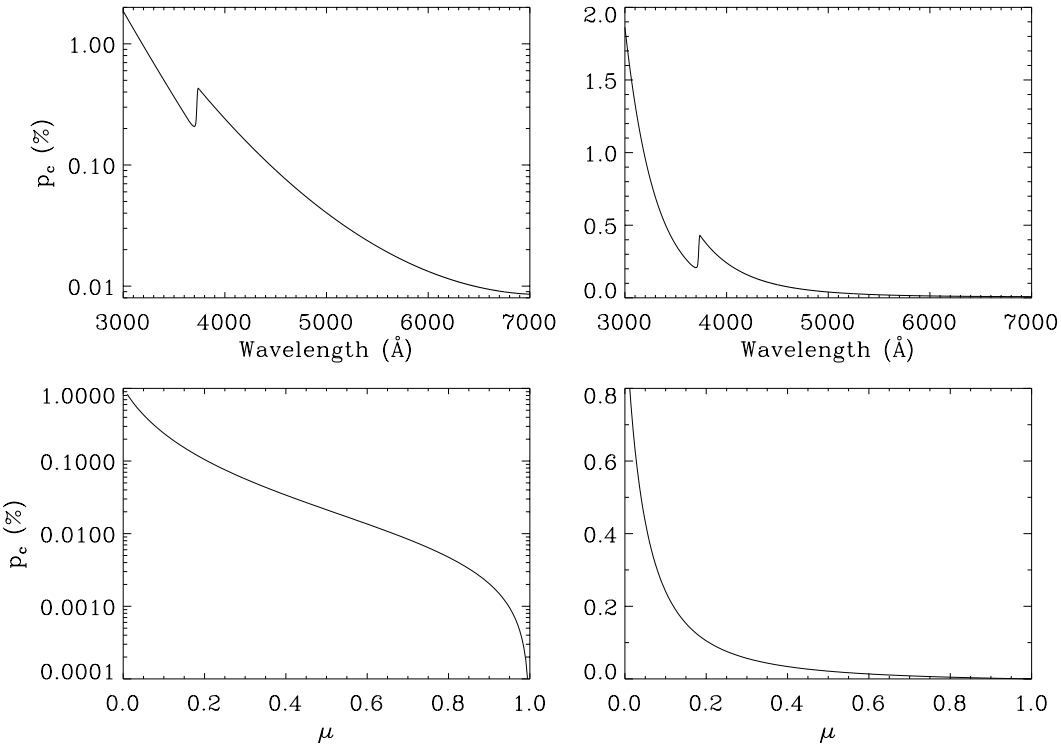

Fig. 7. Overview of the functional behavior of the empirically determined continuum polarization p_c. The two upper panels give the wavelength variation of p_c for $\mu = 0.1$, in logarithmic and linear scales. The curves are the same as the central polynomial curve in Fig. 5. The two bottom panels give the center-to-limb variation of p_c for $\lambda = 4000$ Å, in logarithmic and linear scales.

photons from the other opacity sources. The dominating opacity is from H^-, but radiative absorption in the bound-bound and bound-free Balmer transitions becomes important as we approach the Balmer series limit. The Balmer jump that results from these Balmer absorptions is shifted from the series limit towards longer wavelengths due to pressure broadening of the high atomic levels from the statistical Stark effect. Our simplified treatment of this pressure broadening can approximately reproduce the shift but not the shape (abruptness) of the observed Balmer jump.

The polarization amplitude scales with the anisotropy of the radiation field. This anisotropy increases rather steeply as we go towards shorter wavelengths, and it exhibits a Balmer jump that is also shifted to longer wavelengths with respect to the series limit. The Balmer jump in the continuum polarization p_c is however determined almost exclusively by the Balmer jump in the effective, intrinsic polarizability $W_{2,\mathrm{eff}}$, not by the Balmer jump in the anisotropy factor (k_G). The Balmer jump in $W_{2,\mathrm{eff}}$ occurs when the bound-bound radiative absorption in the Balmer lines overtakes the Lyman scattering opacity and starts to become comparable to the H^- opacity. The detailed modelling of the effective Balmer jump will remain a challenge for future pressure broadening theories and of general interest for the physics of stellar atmospheres.

The empirical value of the continuum polarization and its wavelength variation over the range 3161−6995 Å could be determined for disk position $\mu = 0.1$ from Gandorfer's three volumes of the Second Solar Spectrum. Since the zero point of the polarization scale is basically unknown in these observations, it had to be determined together with the continuum polarization via a model for the behavior of the depolarizing lines in the Second Solar Spectrum. Parameter studies show that the results for the continuum polarization are not very sensitive to the details of this model. Still we have explored how the model uncertainties affect the results and added this influence to the general noise to obtain an estimate of the accuracy (as a function of wavelength) with which the continuum polarization p_c has been determined. It is surprising that it is possible to determine p_c rather well even in the red part of the spectrum, where the polarization amplitude is as low as 10^{-4}. However, the range between 3730 and 4090 Å could not be used because it is dominated by strong line polarization, in particular from the CN molecule, from the Ca II K and H lines, and from strongly polarizing lines of Fe I and Sr II.

The empirically determined p_c is found to lie systematically lower than the values previously obtained from radiative-transfer modelling (for $\lambda > 4000$ Å). The radiative-transfer theory needs to be revisited to identify the origin of this discrepancy. Potentially the observed continuum polarization may be used to constrain the model atmospheres, in a different way as compared with the constraints imposed by spectral intensity data.

The main strength of the present data set is the large wavelength range over which the wavelength variation of p_c could be determined. The main weakness is the considerable range of uncertainty in the values, much due to the statistical nature of the extraction procedure and the ubiquitous contamination from intrinsic line polarization. Therefore the constraints on

model atmospheres that the current data set provides are crude and need to be much improved upon in future work.

Although current radiative-transfer modelling thus fails to properly reproduce the polarization amplitudes, it is likely that the relative shape of the center-to-limb variation is predicted well by such modelling. If we use the so predicted relative shape functions and scale them with the observed values of the continuum polarization for $\mu = 0.1$, we obtain a semi-empirical representation of p_c that covers all wavelengths and μ values. This is of great value to have as a tool in the reduction of any polarimetric observations of the Second Solar Spectrum, since the *absolute* position of the zero point of the polarization scale cannot be determined in the observations with a precision that can come close to the *relative* polarimetric precision. We are now in a position to overcome this problem. With our new tool we may fit the observed continuum to the semi-empirical values for p_c at the respective wavelength and μ position and thereby be able to determine the absolute polarization scale with much improved precision.

Acknowledgements. I am grateful to Hans Martin Schmid for illuminating discussions, and to Achim Gandorfer for providing me with the complete data set for the three volumes of his Atlas of the Second Solar Spectrum. The observations for this atlas were done with the ZIMPOL polarimetric equipment at IRSOL (Istituto Ricerche Solari Locarno) for Volumes I and II, and at the National Solar Observatory/Kitt Peak for Volume III. The engineering group at ETH Zurich (Peter Povel, Peter Steiner, Urs Egger, Frieder Aebersold, Stefan Hagenbuch) built the ZIMPOL system and provided the technical support, financially supported by the Swiss Nationalfonds, grant No. 20-64945.01. IRSOL has been financially supported by the canton of Ticino, the city of Locarno, ETH Zurich, and the Swiss Nationalfonds. NSO is one of the National Optical Astronomy Observatories, which are operated by the Association of Universities for Research in Astronomy, Inc. (AURA) under cooperative agreement with the National Science Foundation. I also like to thank the anonymous referee for thoughtful suggestions.

References

Baschek, B., & Scholz, M. 1982, in Vol. 2 on Astronomy and Astrophysics, Subvolume b on Stars and Star Clusters, ed. K. Schaifers, & H. H. Voigt, Landolt-Börnstein Numerical Data and Functional Relationships in Science and Technology (Springer), 104

Berdyugina, S. V., Stenflo, J. O., & Gandorfer, A. 2002, A&A, 388, 1062

Bommier, V., & Stenflo, J. O. 1999, A&A, 350, 327

Chandrasekhar, S., & Breen, F. H. 1946, ApJ, 104, 430

Débarbat, S., Dumont, S., & Pecker, J.-C. 1970, A&A, 8, 231

Dumont, S., & Pecker, J.-C. 1971, A&A, 10, 118

Fluri, D. M., & Stenflo, J. O. 1999, A&A, 341, 902

Fluri, D. M., & Stenflo, J. O. 2003, A&A, 398, 763

Gandorfer, A. 2000, The Second Solar Spectrum, Vol. I: 4625 Å to 6995 Å (Zurich: VdF)

Gandorfer, A. 2002, The Second Solar Spectrum, Vol. II: 3910 Å to 4630 Å (Zurich: VdF)

Gandorfer, A. 2004, The Second Solar Spectrum, Vol. III: 3161 Å to 3913 Å, in preparation

Green, L. C., Rush, P. P., & Chandler, C. D. 1957, ApJS, 3, 37

Inglis, D. R., & Teller, E. 1939, ApJ, 90, 439

Ivanov, V. V. 1991, in Stellar Atmospheres: Beyond Classical Models, ed. L. Crivellari, I. Hubeny, & D. G. Hummer, Proc. NATO (Dordrecht: Kluwer), 81

Karzas, W. J., & Latter, R. 1961, ApJS, 6, 167

Kramers, H. A. 1923, Phil. Mag., 46, 836

Leroy, J. L. 1972, A&A, 19, 287

Leroy, J. L. 1977, in Measurements and Interpretation of Polarization Arising in the Solar Chromosphere and Corona, ed. J. O. Stenflo, Rep. Obs. Lund No. 12, Sweden, 161

Menzel, D. H., & Pekeris, C. L. 1935, MNRAS, 96, 77

Mickey, D. L., & Orral, F. Q. 1974, A&A, 31, 179

Neckel, H. 1996, Sol. Phys., 167, 9

Pierce, K. 2000, in Allen's Astrophysical Quantities, 4th ed., ed. A. N. Cox (Springer), 355

Povel, H. 1995, Optical Engineering, 34, 1870

Stenflo, J. O. 1982, Sol. Phys., 80, 209

Stenflo, J. O. 1994, Solar Magnetic Fields – Polarized Radiation Diagnostics (Dordrecht: Kluwer)

Stenflo, J. O. 1997, A&A, 324, 344

Stenflo, J. O., & Keller, C. U. 1997, A&A 321, 927

Stenflo, J. O., Twerenbold, D., & Harvey, J. W. 1983a, A&AS, 52, 161

Stenflo, J. O., Twerenbold, D., Harvey, J. W., & Brault, J. W. 1983b, A&AS, 54, 505

Stenflo, J. O., Keller, C. U., & Gandorfer, A. 1998, A&A, 329, 319

Unsöld, A. 1955, Physik der Sternatmosphären, 2nd ed. (Springer)

Wiehr, E. 1975, A&A, 38, 303

Wiese, W. L., Smith, M. W., & Glennon, B. M. 1966, NSRDS-NBS 4, Ref. Data Ser., Atomic Transition Probabilities, Vol. I